Research Article | Vol. 9, No. 9 | 1 Sep 2018 | BIOMEDICAL OPTICS EXPRESS 4413
Biomedical Optics EXPRESS

Comparative study of the imaging contrasts of Mueller matrix derived parameters between transmission and backscattering polarimetry

TENG LIU,[1,2,6] TAO SUN,[1,3,6] HONGHUI HE,[1,7] SHAOXIONG LIU,[5] YANG DONG,[1,3] JIAN WU,[1] AND HUI MA[1,2,4,8]

[1]*Guangdong Research Center of Polarization Imaging and Measurement Engineering Technology, Shenzhen Key Laboratory for Minimal Invasive Medical Technologies, Institute of Optical Imaging and Sensing, Graduate School at Shenzhen, Tsinghua University, Shenzhen 518055, China*
[2]*Department of Physics, Tsinghua University, Beijing 100084, China*
[3]*Department of Biomedical Engineering, Tsinghua University, Beijing 100084, China*
[4]*Center for Precision Medicine and Healthcare, Tsinghua-Berkeley Shenzhen Institute, Shenzhen, China*
[5]*Shenzhen Sixth People's Hospital (Nanshan Hospital), Huazhong University of Science and Technology Union Shenzhen Hospital, Shenzhen 518052, China*
[6]*These authors contributed equally to this work.*
[7]*he.honghui@sz.tsinghua.edu.cn*
[8]*mahui@tsinghua.edu.cn*

Abstract: Mueller matrix polarimetry is a potentially powerful tool for biomedical diagnosis. Recently, the transmission Mueller matrix microscope and backscattering Mueller matrix endoscope were developed and applied to various pathological samples. However, a comparative study of imaging contrasts of Mueller matrix derived parameters between transmission and backscattering measurements is still needed to help decide which information obtained from transmission Mueller matrix microscope can be directly applied to *in vivo* Mueller matrix imaging. Here, to compare the imaging contrasts of Mueller matrix derived parameters between transmission and backscattering polarimetry, we measure porcine liver tissue samples and human breast carcinoma tissue specimens. The experiments and corresponding Monte Carlo stimulation results demonstrate that the backscattering and transmission retardance-related Mueller matrix parameters have very similar contrasts to characterize the anisotropic and isotropic structures of pathological tissues, meaning that the conclusions made from Mueller matrix microscopic imaging based on retardance can also be helpful to guide the *in situ* backscattering Mueller matrix polarimetric diagnosis. However, the values and contrasts of depolarization-related Mueller matrix parameters have some differences between transmission and backscattering polarimetry.

OCIS codes: (110.5405) Polarimetric imaging; (290.5855) Scattering, polarization; (170.3880) Medical and biological imaging; (120.5410) Polarimetry.

References and links

1. J. Ferlay, I. Soerjomataram, R. Dikshit, S. Eser, C. Mathers, M. Rebelo, D. M. Parkin, D. Forman, and F. Bray, "Cancer incidence and mortality worldwide: sources, methods and major patterns in GLOBOCAN 2012," Int. J. Cancer **136**(5), E359–E386 (2015).
2. R. L. Siegel, K. D. Miller, and A. Jemal, "Cancer statistics, 2016," CA Cancer J. Clin. **66**(1), 7–30 (2016).
3. J. Niederhuber, J. Armitage, J. Doroshow, M. Kastan, and J. Tepper, *Abeloff's Clinical Oncology E-Book* (Elsevier Health Sciences, 2013), Chap. 17.
4. American Society of Clinical Oncology, "Stage of cancer," Available from: https://www.cancer.net/navigating-cancer-care/diagnosing-cancer/stages-cancer.
5. Cancer Research UK, "Spot cancer early," Available from: https://www.cancerresearchuk.org/about-cancer/cancer-symptoms/why-is-early-diagnosis-important.
6. A. Golaraei, L. Kontenis, R. Cisek, D. Tokarz, S. J. Done, B. C. Wilson, and V. Barzda, "Changes of collagen ultrastructure in breast cancer tissue determined by second-harmonic generation double Stokes-Mueller polarimetric microscopy," Biomed. Opt. Express **7**(10), 4054–4068 (2016).

#334600 https://doi.org/10.1364/BOE.9.004413
Journal © 2018 Received 6 Jun 2018; revised 16 Aug 2018; accepted 17 Aug 2018; published 22 Aug 2018

Biomedical Optics EXPRESS

7. B. Kunnen, C. Macdonald, A. Doronin, S. Jacques, M. Eccles, and I. Meglinski, "Application of circularly polarized light for non-invasive diagnosis of cancerous tissues and turbid tissue-like scattering media," J. Biophotonics **8**(4), 317–323 (2015).
8. L. Qiu, D. K. Pleskow, R. Chuttani, E. Vitkin, J. Leyden, N. Ozden, S. Itani, L. Guo, A. Sacks, J. D. Goldsmith, M. D. Modell, E. B. Hanlon, I. Itzkan, and L. T. Perelman, "Multispectral scanning during endoscopy guides biopsy of dysplasia in Barrett's esophagus," Nat. Med. **16**(5), 603–606 (2010).
9. S. L. Jacques, J. C. Ramella-Roman, and K. Lee, "Imaging skin pathology with polarized light," J. Biomed. Opt. **7**(3), 329–340 (2002).
10. V. Backman, M. B. Wallace, L. T. Perelman, J. T. Arendt, R. Gurjar, M. G. Müller, Q. Zhang, G. Zonios, E. Kline, J. A. McGilligan, S. Shapshay, T. Valdez, K. Badizadegan, J. M. Crawford, M. Fitzmaurice, S. Kabani, H. S. Levin, M. Seiler, R. R. Dasari, I. Itzkan, J. Van Dam, and M. S. Feld, "Detection of preinvasive cancer cells," Nature **406**(6791), 35–36 (2000).
11. S. Alali and A. Vitkin, "Polarized light imaging in biomedicine: emerging Mueller matrix methodologies for bulk tissue assessment," J. Biomed. Opt. **20**(6), 061104 (2015).
12. N. Ghosh and I. A. Vitkin, "Tissue polarimetry: concepts, challenges, applications, and outlook," J. Biomed. Opt. **16**(11), 110801 (2011).
13. V. V. Tuchin, "Polarized light interaction with tissues," J. Biomed. Opt. **21**(7), 071114 (2016).
14. J. Qi and D. S. Elson, "Mueller polarimetric imaging for surgical and diagnostic applications: a review," J. Biophotonics **10**(8), 950–982 (2017).
15. O. Arteaga, M. Baldrís, J. Antó, A. Canillas, E. Pascual, and E. Bertran, "Mueller matrix microscope with a dual continuous rotating compensator setup and digital demodulation," Appl. Opt. **53**(10), 2236–2245 (2014).
16. J. Vizet, J. Rehbinder, S. Deby, S. Roussel, A. Nazac, R. Soufan, C. Genestie, C. Haie-Meder, H. Fernandez, F. Moreau, and A. Pierangelo, "In vivo imaging of uterine cervix with a Mueller polarimetric colposcope," Sci. Rep. **7**(1), 2471 (2017).
17. J. Qi and D. S. Elson, "A high definition Mueller polarimetric endoscope for tissue characterisation," Sci. Rep. **6**(1), 25953 (2016).
18. Y. Fu, Z. Huang, H. He, H. Ma, and J. Wu, "Flexible 3x3 Mueller matrix endoscope prototype for cancer detection," IEEE T. Instrum. Meas. (2018).
19. B. Saikia, K. Gupta, and U. N. Saikia, "The modern histopathologist: in the changing face of time," Diagn. Pathol. **3**(1), 25–29 (2008).
20. Y. Wang, H. He, J. Chang, C. He, S. Liu, M. Li, N. Zeng, J. Wu, and H. Ma, "Mueller matrix microscope: a quantitative tool to facilitate detections and fibrosis scorings of liver cirrhosis and cancer tissues," J. Biomed. Opt. **21**(7), 071112 (2016).
21. J. Zhou, H. He, Z. Chen, Y. Wang, and H. Ma, "Modulus design multiwavelength polarization microscope for transmission Mueller matrix imaging," J. Biomed. Opt. **23**(1), 1–8 (2018).
22. Y. Dong, J. Qi, H. He, C. He, S. Liu, J. Wu, D. S. Elson, and H. Ma, "Quantitatively characterizing the microstructural features of breast ductal carcinoma tissues in different progression stages by Mueller matrix microscope," Biomed. Opt. Express **8**(8), 3643–3655 (2017).
23. J. Chang, H. He, Y. Wang, Y. Huang, X. Li, C. He, R. Liao, N. Zeng, S. Liu, and H. Ma, "Division of focal plane polarimeter-based 3 × 4 Mueller matrix microscope: a potential tool for quick diagnosis of human carcinoma tissues," J. Biomed. Opt. **21**(5), 056002 (2016).
24. C. He, H. He, J. Chang, Y. Dong, S. Liu, N. Zeng, Y. He, and H. Ma, "Characterizing microstructures of cancerous tissues using multispectral transformed Mueller matrix polarization parameters," Biomed. Opt. Express **6**(8), 2934–2945 (2015).
25. H. He, M. Sun, N. Zeng, E. Du, S. Liu, Y. Guo, J. Wu, Y. He, and H. Ma, "Mapping local orientation of aligned fibrous scatterers for cancerous tissues using backscattering Mueller matrix imaging," J. Biomed. Opt. **19**(10), 106007 (2014).
26. E. Du, H. He, N. Zeng, M. Sun, Y. Guo, J. Wu, S. Liu, and H. Ma, "Mueller matrix polarimetry for differentiating characteristic features of cancerous tissues," J. Biomed. Opt. **19**(7), 076013 (2014).
27. A. Pierangelo, A. Nazac, A. Benali, P. Validire, H. Cohen, T. Novikova, B. H. Ibrahim, S. Manhas, C. Fallet, M. R. Antonelli, and A. D. Martino, "Polarimetric imaging of uterine cervix: a case study," Opt. Express **21**(12), 14120–14130 (2013).
28. A. Pierangelo, S. Manhas, A. Benali, C. Fallet, J. L. Totobenazara, M. R. Antonelli, T. Novikova, B. Gayet, A. De Martino, and P. Validire, "Multispectral Mueller polarimetric imaging detecting residual cancer and cancer regression after neoadjuvant treatment for colorectal carcinomas," J. Biomed. Opt. **18**(4), 046014 (2013).
29. P. Shukla and A. Pradhan, "Mueller decomposition images for cervical tissue: potential for discriminating normal and dysplastic states," Opt. Express **17**(3), 1600–1609 (2009).
30. W. Wang, L. G. Lim, S. Srivastava, J. S. Yan, A. Shabbir, and Q. Liu, "Roles of linear and circular polarization properties and effect of wavelength choice on differentiation between ex vivo normal and cancerous gastric samples," J. Biomed. Opt. **19**(4), 046020 (2014).
31. J. Jagtap, S. Chandel, N. Das, J. Soni, S. Chatterjee, A. Pradhan, and N. Ghosh, "Quantitative Mueller matrix fluorescence spectroscopy for precancer detection," Opt. Lett. **39**(2), 243–246 (2014).
32. M. Sun, H. He, N. Zeng, E. Du, Y. Guo, S. Liu, J. Wu, Y. He, and H. Ma, "Characterizing the microstructures of biological tissues using Mueller matrix and transformed polarization parameters," Biomed. Opt. Express **5**(12), 4223–4234 (2014).

Biomedical Optics EXPRESS

33. M. Dubreuil, P. Babilotte, L. Martin, D. Sevrain, S. Rivet, Y. Le Grand, G. Le Brun, B. Turlin, and B. Le Jeune, "Mueller matrix polarimetry for improved liver fibrosis diagnosis," Opt. Lett. **37**(6), 1061–1063 (2012).
34. T. Novikova, A. Pierangelo, S. Manhas, A. Benali, P. Validire, B. Gayet, and A. De Martino, "The origins of polarimetric image contrast between healthy and cancerous human colon tissue," Appl. Phys. Lett. **102**(24), 241103 (2013).
35. H. He, C. He, J. Chang, D. Lv, J. Wu, C. Duan, Q. Zhou, N. Zeng, Y. He, and H. Ma, "Monitoring microstructural variations of fresh skeletal muscle tissues by Mueller matrix imaging," J. Biophotonics **10**(5), 664–673 (2017).
36. Y. Dong, H. He, W. Sheng, J. Wu, and H. Ma, "A quantitative and non-contact technique to characterise microstructural variations of skin tissues during photo-damaging process based on Mueller matrix polarimetry," Sci. Rep. **7**(1), 14702 (2017).
37. R. M. A. Azzam, "Photopolarimetric measurement of the Mueller matrix by Fourier analysis of a single detected signal," Opt. Lett. **2**(6), 148–150 (1978).
38. D. H. Goldstein and R. A. Chipman, "Error analysis of a Mueller matrix polarimeter," J. Opt. Soc. Am. A **7**(4), 693–700 (1990).
39. J. Qi, H. He, J. Lin, Y. Dong, D. Chen, H. Ma, and D. S. Elson, "Assessment of tissue polarimetric properties using Stokes polarimetric imaging with circularly polarized illumination," J. Biophotonics **11**(4), e201700139 (2018).
40. S. Y. Lu and R. A. Chipman, "Interpretation of Mueller matrices based on polar decomposition," J. Opt. Soc. Am. A **13**(5), 1106–1113 (1996).
41. H. He, J. Chang, C. He, and H. Ma, "Transformation of full 4×4 Mueller matrices: a quantitative technique for biomedical diagnosis," Proc. SPIE **9707**, 97070K (2016).
42. P. Li, D. Lv, H. He, and H. Ma, "Separating azimuthal orientation dependence in polarization measurements of anisotropic media," Opt. Express **26**(4), 3791–3800 (2018).
43. T. Yun, N. Zeng, W. Li, D. Li, X. Jiang, and H. Ma, "Monte Carlo simulation of polarized photon scattering in anisotropic media," Opt. Express **17**(19), 16590–16602 (2009).
44. E. Du, H. He, N. Zeng, Y. Guo, R. Liao, Y. He, and H. Ma, "Two-dimensional backscattering Mueller matrix of sphere-cylinder birefringence media," J. Biomed. Opt. **17**(12), 126016 (2012).
45. X. Wang and L. V. Wang, "Propagation of polarized light in birefringent turbid media: a Monte Carlo study," J. Biomed. Opt. **7**(3), 279–290 (2002).
46. M. F. G. Wood, N. Ghosh, E. H. Moriyama, B. C. Wilson, and I. A. Vitkin, "Proof-of-principle demonstration of a MMD method for polarized light tissue characterization in vivo," J. Biomed. Opt. **14**(1), 014029 (2009).
47. N. Ortega-Quijano, F. Fanjul-Vélez, I. Salas-Garcia, and J. L. Arce-Diego, "Polarized light Monte Carlo analysis of birefringence-induced depolarization in biological tissues," Proc. of OSA-SPIE **8803**, 88030T–1 (2013).
48. T. Liu, H. He, Y. Dong, and H. Ma, "Quantitative detection of breast ductal carcinoma tissues at different progression stages using Mueller matrix microscope," Proc. SPIE **10493**, 10493O (2018).

1. Introduction

Recently, the number of new cancer cases and deaths is increasing rapidly worldwide [1,2]. Normally, cancer tissues can be divided into different progression stages such as *in situ* and invasive types according to their microstructural features [3,4]. A large number of cancer statistics have indicated that the survival of cancer patients who diagnosed at an early stage can increase prominently compared with patients diagnosed at an advanced stage [1,5]. Obviously early diagnosis is very crucial for the treatment of cancer patients. Nowadays, optical techniques are more and more widely used as non-invasive and *in vivo* tools to cancer diagnosis [6,7]. Among the emerging novel optical methods, Mueller matrix polarimetry has shown some distinctive advantages suitable for diagnosis. Firstly, Mueller matrix polarimetry can help to improve the imaging contrast of the superficial layers of tissues, where more than 85% of cancers are originated from [8–10]. Secondly, as a label-free technique, Mueller matrix polarimetry can provide abundant structural information of the abnormal tissue areas [11–14]. Last, by adding appropriate polarization components, Mueller matrix polarimetry can be easily combined with existing optical imaging equipments such as endoscope and microscope [15–17]. Some studies showed that the Mueller matrix endoscope has the potential to become a powerful *in vivo* early-stage cancer diagnosis tool [16,18].

The gold standard of cancer diagnosis currently is the pathological evaluation of stained tissue slices using optical microscopy by experienced pathologists [19]. Recently, by adding the polarization states generator and analyzer (PSG and PSA) to a commercial transmission optical microscope, we developed a Mueller matrix microscope for pathological observations [20,21]. This novel microscope and parameters derived from Mueller matrix elements were

Biomedical Optics EXPRESS

applied to various pathological samples including human breast carcinoma [22], liver cirrhosis and cancer [20,23], cervical cancer [24], thyroid cancer [25], and skin cancer tissues [26]. The imaging results demonstrated that, the Mueller matrix polar decomposition (MMPD) and Mueller matrix transformation (MMT) parameters can be helpful for the quantitative detecting and staging of cancerous tissues [27–31]. Especially, experiments and Monte Carlo simulations revealed that the retardance and depolarization related Mueller matrix derived parameters can be suitable to indentify the changes of fibrous microstructures and small particles during the pathological development process, respectively [32–36]. However, the trajectories of transmission and backscattered photons from tissues are different. A comparative study of imaging contrasts of these Mueller matrix derived parameters between transmission and backscattering measurements is still needed. It will be an important guidance to decide which information obtained from transmission Mueller matrix microscope can be directly applied to *in vivo* Mueller matrix imaging including endoscope.

In this paper, to compare the Mueller matrix parameters images between transmission and backscattering measurements, we firstly prepare porcine liver tissue samples with appropriate thickness, which can be imaged both in forward and backward configurations. Then for a further study, we compare the transmission imaging results of thin slice and backscattering imaging results of bulk sample from the same human breast carcinoma tissue specimen. For a deeper understanding, we also adopt Monte Carlo (MC) stimulations based on the sphere birefringence model to analyze the information carried by the transmission and backscattered polarized photons. The experiments and stimulation results show that, the backscattering and transmission retardance-related Mueller matrix imaging parameters have similar contrasts to characterize the anisotropic and isotropic structures of tissues, which means the conclusions made from Mueller matrix microscopic imaging based on retardance can also be helpful to guide the *in situ* backscattering Mueller matrix polarimetric diagnosis. However, for depolarization-related Mueller matrix parameters their values and contrasts have some differences between transmission and backscattering polarimetry.

2. Methods and materials

2.1 Experimental setup and tissue samples

The Mueller matrix measurement setup used in this study is based on a dual-rotating retarder polarimeter as shown in Fig. 1(a). The illuminant is a monochrome LED (3 W, 632.8 nm, $\Delta\lambda$ = 20 nm, Cree, China). The polarization state generator (PSG) is composed of a convex lens (L1, Thorlabs, USA), a fixed linear polarizer (P1, GCL-050003, extinction ratio 500:1, Daheng Optics, China) and a rotatable quarter-wave plate (R1, Daheng Optics, China). Analogously, the polarization state analyzer (PSA) is also composed of a convex lens (L2/L3, focal lengths 5 cm, Thorlabs, USA), a fixed linear polarizer (P2/P3, GCL-050003, extinction ratio 500:1, Daheng Optics, China) and a rotatable quarter-wave plate (R2/R3, Daheng Optics, China). The polarization images of the sample are recorded by a 12-bit CCD camera (CCD1/CCD2, QImaging 32-0112A, Canada). During the measurement, the polarizers (P1, P2, P3) are fixed in the horizontal direction, while the quarter-wave plates (R1, R2, R3) rotate with the fixed rates $\phi_2 = 5\phi_1$. Then the Mueller matrix elements can be calculated by using the Fourier coefficients [37,38]. The Fourier series intensities are given by Eq. (1).

$$I = \alpha_0 + \sum_{n=1}^{12} (\alpha_n \cos 2n\phi_1 + \beta_n \sin 2n\phi_1) \tag{1}$$

The setup was calibrated by measuring the Mueller matrices of standard samples such as air and phantom, and the experimental results showed that the maximum error of the setup is about 1%. It can be observed from Fig. 1(a) that by changing the position of the PSA arm, both the backward and transmission Mueller matrices of the sample can be obtained. In this

Biomedical Optics EXPRESS

study, we take porcine liver and human breast carcinoma tissues as the experimental samples. In our previous studies it is found that porcine liver contains both anisotropic connective tissues and isotropic hepatic lobule tissues, which have very different polarization properties [32,39]. Also, the distribution change of fibrous structures is an important feature of human breast carcinoma samples in different progression stages [6,22]. The porcine liver sample and human breast carcinoma tissue sample are shown in Fig. 1(b) and (c), respectively. Here the porcine liver tissue was cut into sample with appropriate thickness, from which both the backscattered and transmission images can be obtained. The human breast carcinoma tissue samples were provided by Shenzhen Sixth People's (Nanshan) Hospital. The thickness of the fresh specimen of breast carcinoma is 0.3 cm. The dimensions of this specimen are about 1.5 cm × 1.5 cm × 0.3 cm. In this study we measured the backscattering Mueller matrix of fresh human breast carcinoma tissue specimen, then prepared the unstained 12-μm-thick tissue slices of the same specimen for transmission Mueller matrix imaging, and H-E stained 4-μm-thick tissue slices for pathological observations. This work was approved by the Ethics Committee of the Shenzhen Sixth People's (Nanshan) Hospital, and Ethics Committee of the Graduate School at Shenzhen, Tsinghua University.

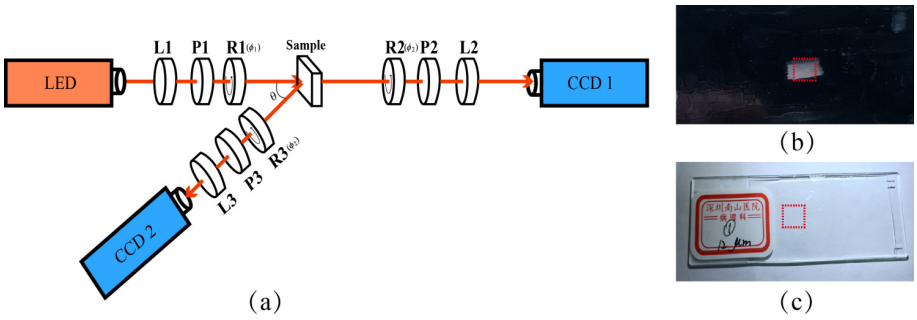

Fig. 1. (a) Schematic of experimental setup for the Mueller matrix measurement. P1, P2, P3: polarizer; R1, R2, R3: quarter-wave plate; L1, L2, L3: lens. For backscattering measurement, the oblique incident angle θ is about 12 degree to avoid the surface reflection from the sample. The diameter of the illumination area is about 1.8 cm; (b) Porcine liver sample used in this study, the thickness is about 40 μm. The red square area of 0.8 cm × 0.8 cm indicates the imaging region; (c) Human breast carcinoma tissue slice used in the study. The red square area of 0.8 cm × 0.8 cm indicates the imaging region.

2.2 Mueller matrix transformation (MMT) and Mueller matrix polar decomposition (MMPD) parameters

Mueller matrix elements can reveal abundant microstructural and optical information of biological tissues. However, individual Mueller matrix element can hardly show the structural characteristics of the sample comprehensively. In our previous studies, the structural properties of tissue samples were mainly represented using parameters derived from 16 Mueller matrix elements, especially the MMT parameters *1-b*, t_3, and the MMPD parameters Δ, δ.

$$\Delta = 1 - \frac{\left|tr(m_\Delta)\right|}{3} = 1 - \frac{\left|tr(M_\Delta) - 1\right|}{3}$$
$$R = \cos^{-1}\left[\frac{tr(M_R)}{2} - 1\right] \tag{2}$$

For the MMPD parameters shown as Eq. (2) [40], Δ and R represent depolarization and retardation of the medium, respectively. It should be noticed that the retardation is composed of linear retardation and circular retardation. In this study, we mainly analyze the linear retardation which is one of the main properties of biological tissues as represented by Eq. (3):

Biomedical Optics EXPRESS

$$\delta = \cos^{-1}\left\{\sqrt{\left[M_R(2,2)+M_R(3,3)\right]^2+\left[M_R(3,2)-M_R(2,3)\right]^2}-1\right\} \quad (3)$$

Correspondingly, we also adopt the MMT parameters *1-b* and t_3 which describe the depolarization and retardation properties of the samples [41,42]. In previous publications parameter *b* representing polarizance of the media was usually used, here to compare with Δ we use *1-b*, which represents depolarization of the sample.

$$1-b = 1-\frac{m_{22}+m_{33}}{2}$$
$$t_3 = \sqrt{(m_{42})^2+(m_{34})^2} \quad (4)$$

2.3 Monte Carlo (MC) simulation

To compare the Mueller matrix derived parameters between transmission and backscattered measurements more comprehensively, the MC simulations based on the sphere-birefringence model (SBM) is used here to analyze the behavior of polarized photons propagating in the biological tissues [43,44]. In this study, the model contains birefringent interstitial medium, together with spherical scatterers to mimic cell nuclei and organelles. The details of parameters used in MC simulations will be introduced in the following sections.

3. Result and discussion

3.1 Mueller matrix parameters of porcine liver tissues

Figures 2(a)-(b) are the experimental 2D images of transmission and backscattering Mueller matrices of the same porcine liver tissue respectively. We can see that they show some similar characteristics, especially in the m24, m34, m42 and m43 elements. In our previous experimental and Monte Carlo simulation studies, it has been found that the main characteristic structural features of scattering samples can be obtained from the Mueller matrix elements. For example, the depolarization can be calculated by using the diagonal elements m22, m33 and m44, and the central elements m22, m23, m32 and m33 are closely related to the total anisotropic properties of samples [32]. Moreover, the magnitude of the lower right elements m24, m34, m42 and m43 can be used to obtain the birefringence distributions, while the magnitude of the upper left elements m12, m13, m21 and m31 can be used to extract the diattenuation distributions [35]. Thus, we can summarize from Fig. 2 that: (1) For the diagonal elements m22, m33 and m44 of both the transmission and backscattering Mueller matrices of the liver tissues, they show similar imaging contrast. Especially, the elements m22 and m33 in both Figs. 2(a) and 2(b) have similar values in most parts but show differences in some areas, indicating that there are anisotropic connective tissues surrounded by isotropic hepatic lobule tissues in the liver samples; (2) The values of the diagonal m22, m33 and m44 elements for the transmission Mueller matrix are larger than that for the backscattering Mueller matrix, which indicates that the depolarization property of liver tissues in backward measurement is more obvious; (3) The lower right elements m24, m34, m42 and m43, which mainly represent the birefringence distributions of the samples, have prominent latticed patterns both in transmission and backward measurements. For the comparison, we chose the same laboratory coordinate system for both the backscattering and transmission measurements without the sign convention. In this coordinate system there is an opposite sign of Mueller matrix element m24 or m42 on Figs. 2(a) and 2(b) [39]. The sign convention does not change the values of MMT and MMPD parameters. We can see that the differences between the connective tissues and hepatic lobule tissues of porcine liver are obvious in these elements, showing that the connective tissues surrounding the lobules have prominent birefringence features, which are well preserved in both forward and backward Mueller matrix measurements.

Biomedical Optics EXPRESS

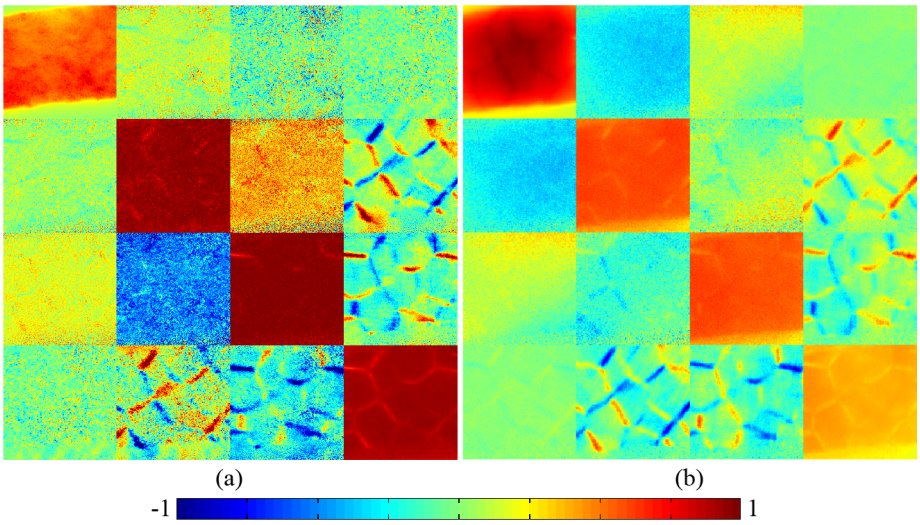

Fig. 2. 2D images of Mueller matrices of porcine liver sample: (a) transmission Mueller matrix; (b) backscattering Mueller matrix. The color bar is from −1 to 1 for m11, m22, m33 and m44, and from −0.2 to 0.2 for other elements. All the matrix elements are normalized by the m11.

From the analyses above we can see that, the 2D images of Mueller matrix elements can reveal a lot of polarization properties and structural information of tissues in both transmission and backscattering measurements. Since the most distinct properties of the porcine liver tissues are the depolarization power and retardance, we calculated the MMT parameters *1-b*, t_3 and MMPD parameters Δ, δ of the samples which are good indicators of the depolarization and retardance respectively. The images of the Mueller matrix derived parameters are shown in Fig. 3(a)-(b). Here the connective tissues in each parameter image were manually segmented from the hepatic lobules by the "imfreehand" function in Matlab according to corresponding pathological observations which are shown in Fig. 3(c)-(f). For clear comparisons, the four parameters shown as Fig. 3(c)-(f) include four images each: (1), (3) connective tissue images in forward and backward measurements respectively; (2), (4) hepatic lobule tissue images in forward and backward measurements respectively. We can learn from Fig. 3 that the depolarization parameters *1-b* (Fig. 3c) and Δ (Fig. 3d), also the retardance parameters t_3 (Fig. 3e) and δ (Fig. 3(f)) have highly similar characteristic features, therefore, we take the MMPD parameters Δ and δ images for the comparative analysis here, the conclusions also hold for the MMT parameters: (1) The contrast of parameter Δ in transmission image (12%, Fig. 3(a)) is slightly more prominent than that in backscattering image (1.5%, Fig. 3(b)), which was also observed in our recent study [39]. However both in forward and backward measurements, the differences of parameter Δ between connective tissues and hepatic lobules are slight, indicating that the depolarization abilities of the connective tissues and hepatic lobules in this porcine liver sample are close. Also, it can be noticed that in backward measurement (Fig. 3d (3)-(4)), the mean values of parameter Δ are much larger than that in forward measurement (Fig. 3d (1)-(2)). That is to say, compared with transmission imaging the depolarization ability of liver tissues in backward measurement is much more significant, which is caused by more photon scattering in thick tissue samples; (2) While for retardance parameter δ (Fig. 3(f)), both in forward (Fig. 3(f) (1)-(2)) and backward (Fig. 3(f) (3)-(4)) measurements, there is an obvious difference in values between connective tissues and hepatic lobule tissues, meaning that the retardance of connective tissues is obviously higher than that of hepatic lobules. Besides, we can also observe that the value distributions of parameter δ of liver tissues in backward measurement are almost the same as those in forward measurement, meaning that the ability of using parameter δ as the indicator

Biomedical Optics EXPRESS

to discriminate anisotropic structures in backward measurement is similar to that in forward measurement. The values of the retardance related Mueller matrix parameters can reveal the density of anisotropic tissues in both transmission and backscattering imaging. Also, the average diattenuation values of the porcine liver connective tissues are 0.0062 in transmission imaging and 0.0063 in backscattering imaging. For the hepatic lobules, the average diattenuation values are 0.0055 in transmission imaging and 0.0058 in backscattering imaging. The very small diattenuation values confirm that the signal from tissue-glass interface had limited influence on the measurement.

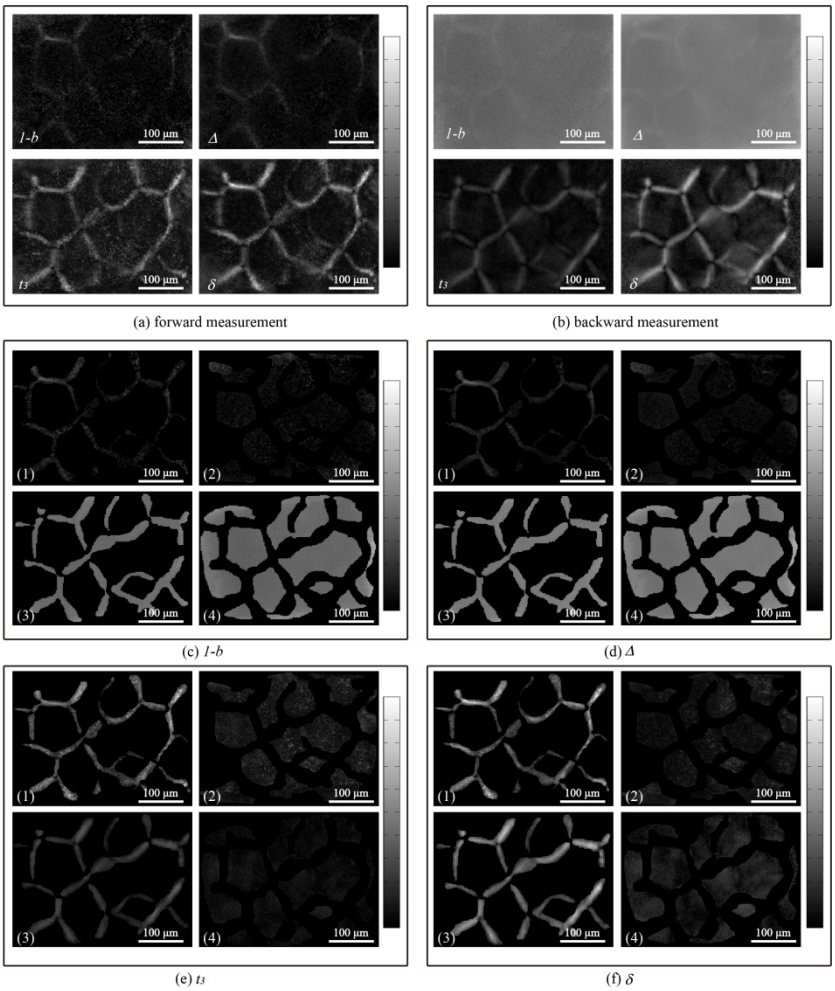

Fig. 3. Images of MMT and MMPD parameters for porcine liver sample in (a) forward measurement and (b) backward measurement; Segmented images of Mueller matrix parameters in forward and backward measurements: (c) *1-b*, (d) *Δ*, (e) t_3, (f) *δ*. For each parameter, the sub-images are: (1) connective tissues in forward measurement; (2) hepatic lobules in forward measurement; (3) connective tissues in backward measurement; (4) hepatic lobules in backward measurement. The grey-scale bar is from 0 to 1 for *1-b* and *Δ* in (b), (c3), (c4), (d3) and (d4). The grey-scale bar is from 0 to 0.5 for other images.

Based on the analysis above, we can conclude that for the porcine liver samples with appropriate thickness to be measured in both forward and backward configurations, the values and contrasts of depolarization Mueller matrix parameters *1-b* and *Δ* have some differences between transmission and backscattering images to differentiate the connective and hepatic lobule tissues. The possible reason of the weak imaging contrast of depolarization parameters

Biomedical Optics EXPRESS

is that, although the hepatic lobule tissues contain more scattering particles, the strong birefringence of the connective tissues can bring the retardance-induced-depolarization for compensation [45–47]. Meanwhile, the clear image contrasts of retardance parameters t_3 and δ can be helpful for distinguishing the anisotropic and isotropic structures in liver tissue sample both in forward and backward measurements. The experimental phenomenon proves that although the trajectories of the backscattered photons are different from the transmitted photons during the propagation in tissues, the main contrasts of the retardance-related Mueller matrix derived parameters between connective tissues and hepatic lobules in porcine liver sample are still retained.

3.2 Mueller Matrix parameters of human breast carcinoma tissues

It was shown in Section 3.1 that for the same tissue sample with appropriate thickness, the ability of Mueller matrix derived parameters to distinguish different microstructures in the forward measurement partially remains in the backward measurement. However, for real applications the thin tissue slices used for transmission microscopic imaging and the bulk tissues for *in vivo* imaging including endoscopic diagnosis are different. Whether the imaging contrast is still there or not is of great practical significance for clinical diagnosis. In our previous studies, we have demonstrated that the transformed Mueller matrix parameters in transmission polarimetry can facilitate the quantitative detection of pathological tissues [20–24]. Here, we measured the backscattering Mueller matrix of fresh human breast carcinoma tissue specimens removed from a patient, then prepared the tissue slices of the same specimens for transmission Mueller matrix imaging and pathological observations.

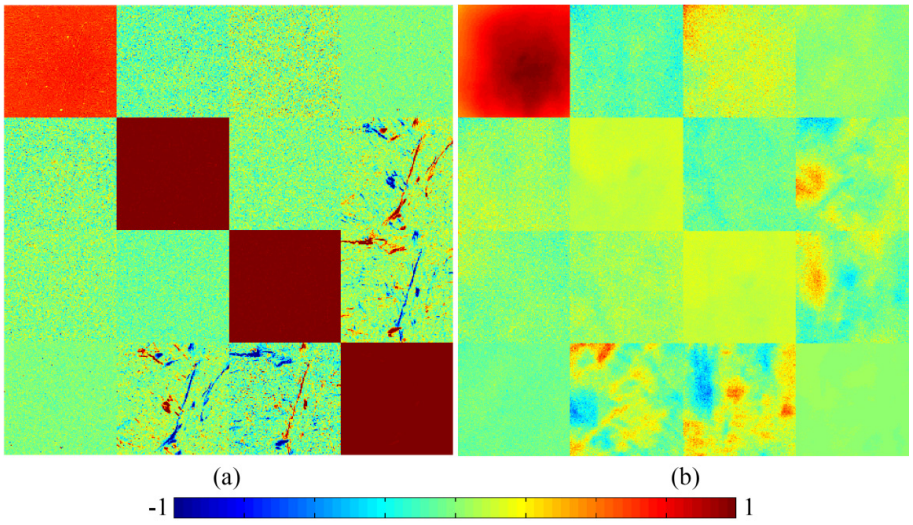

Fig. 4. 2D images of Mueller matrices of human breast carcinoma tissue samples: (a) transmission Mueller matrix of the unstained 12-μm-thick tissue slice; (b) backscattering Mueller matrix of the fresh bulk tissue sample. The color bar is from –1 to 1 for m11, m22, m33 and m44, and from –0.1 to 0.1 for other elements. All the matrix elements are normalized by the m11.

For validation, we compared the transmission Mueller matrix of human breast carcinoma tissue slice (Fig. 4(a)) and the backscattering Mueller matrix of the corresponding bulk fresh breast carcinoma tissue (Fig. 4(b)). It can be observed from Fig. 4 that: (1) The image contrasts are mainly reflected in the m24, m34, m42 and m43 elements, representing prominent birefringence of the breast carcinoma tissues in both forward and backward Mueller matrix imaging; (2) Besides, the larger values of the diagonal elements in Fig. 4(a) compared with those in Fig. 4(b) confirm that for the breast carcinoma tissues, the

Biomedical Optics EXPRESS

transmission Mueller matrix images show less depolarization than the backscattering ones. However, there are very limited image contrast existing in the diagonal elements, or in other words, the depolarization distribution. It should be noted that the specular reflection from rough surface of tissue can influence some pixels of the Mueller matrix image. Here in this study, the oblique incidence in backscattering experimental configuration and relatively flat surface of tissue specimen can help to suppress most of the influence of reflection from rough surface. However, as indicated in [17] for clinical applications such as endoscopic imaging, the pixel saturation due to surface specular reflection should be carefully handled.

For further analysis, we then employed the MMT parameters *1-b,* t_3 and MMPD parameters Δ, δ, which were used and described in Section 3.1, to the breast carcinoma tissue samples. Here the samples were divided into fibers and non-fibrous tissues, according to the observations of experienced pathologist and our previous study [22]. As shown in Fig. 5(a),(d), for each parameter: (1), (2) show the images of fibers and non-fibrous tissues of breast carcinoma sample slices in forward measurement respectively; while (3), (4) show the fibers and non-fibers images of bulk breast carcinoma tissues in backward measurement respectively.

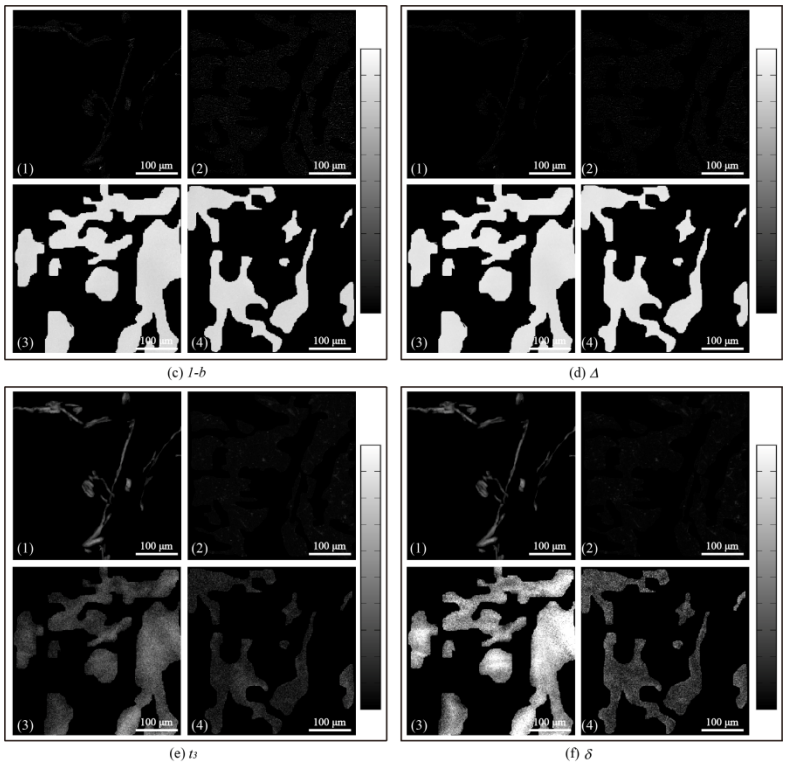

Fig. 5. Images of MMT and MMPD parameters for breast carcinoma samples in forward and backward measurements: (a) *1-b*, (b) Δ, (c) t_3, (d) δ. For each parameter, the sub-images are: (1) fibers in forward measurement; (2) non-fibrous tissues in forward measurement; (3) fibers in backward measurement; (4) non-fibrous tissues in backward measurement. The grey-scale bar are from 0 to 0.1 in (a1), (a2), (b1), (b2), from 0 to 1 in (a3), (a4), (b3), (b4), and from 0 to 0.5 in (c)-(d).

In this section, owing to the similarities between the imaging contrasts of MMT and MMPD parameters, we still select the MMPD parameters Δ and δ for the comparative analysis: (1) In both the forward (Fig. 5(b) 1-2) and backward (Fig. 5(b) 3-4) measurements, there is no prominent difference of the parameter Δ between fibrous and non-fibrous structures in breast carcinoma tissue samples, which confirms that the depolarization power

Biomedical Optics EXPRESS

has a limited ability to distinguish the anisotropic fibers and isotropic non-fibrous tissues here. Also the backscattering images show larger values of depolarization than the transmission images; (2) In forward measurement results shown as Fig. 5(d) 1-2, the values of the retardance parameter δ in fibrous area are obviously higher than that in non-fibrous tissues, indicating that there is a significant difference of retardance between fibers and non-fibrous tissues in breast carcinoma samples for transmission Mueller matrix imaging. Meanwhile, Fig. 5(d) 3-4 also show that the imaging contrast of the parameter δ between these tissues in backward measurement is similar to that in forward measurement, proving the ability of using the retardance parameter to discriminate fibrous and non-fibrous structures in breast carcinoma tissues is maintained in backward measurement. The results shown in Figs. 4 and 5 demonstrate that, for the thin slice and bulk fresh sample of the same pathological tissue, the backscattering and transmission retardance-related Mueller matrix imaging parameters still have similar contrasts to characterize the fibrous and non-fibrous structures, which means that the conclusions made from Mueller matrix microscopic imaging based on retardance can also be helpful to guide the *in situ* backscattering Mueller matrix polarimetry diagnosis. However, due to the limited thickness of tissue slices used for transmission polarimetry, the values of depolarization-related Mueller matrix parameters Δ and *1-b* are much smaller compared with backscattering polarimetry.

3.3 Quantitative analysis of parameters Δ and δ

To compare the forward and backward results more quantitatively, we plot out the frequency distributions histograms (FDH) of the MMPD parameters Δ and δ for porcine liver sample shown as Fig. 6, in which the red solid lines represent connective tissues, while the blue dotted lines represent hepatic lobule tissues. For the parameter Δ in forward measurement (Fig. 6(a)) we can see that the mean value of hepatic lobules is a little smaller than that of connective tissues. Moreover, the value distribution of parameter Δ for hepatic lobules is more concentrated than that of connective tissues: the most concentrated percentage of hepatic lobules ups to 0.189 at the value of 0.03, while the most concentrated percentage of connective tissues is just 0.137 at the value of 0.05. For the backward measurement, as Fig. 6(b) shows both the mean values and distributions of parameter Δ for the connective tissues and hepatic lobules are very close: the most concentrated percentages of the parameter Δ for hepatic lobules and connective tissues are 0.174 at the value of 0.46, and 0.180 at the value of 0.48, respectively. As mentioned above, the slightly larger depolarization of the connective tissues compared with the hepatic lobule tissues may be resulted from the birefringence-induced depolarization effect. From Table 1 we can see the mean values and standard deviations of the parameters in different situations. Using the values presented in Table 1, we can calculate the contrast by Eq. (5):

$$\text{cont.} = \left| \frac{\alpha_{iso} - \alpha_{ani}}{\alpha_{iso} + \alpha_{ani}} \right| \times 100\%. \tag{5}$$

Here α_{iso} and α_{ani} represent mean values of isotropic tissue (hepatic lobules) and anisotropic tissue (connective tissues) respectively. The contrasts of Δ parameter are calculated to be 12% and 1.5% in forward and backward measurements, respectively. It should be noted that there are other different metrics of depolarization (e.g. entropy, purity indices, etc.) which can be helpful to increase the depolarization image contrast. For instance, the contrasts of entropy for parameter Δ of the porcine liver tissues are 38.2% and 35.9% in forward and backward measurements, respectively.

Figure 6(c) and (d) show the FDHs of parameter δ in forward and backward measurements, whose red solid lines represent connective tissues and blue dotted lines represent hepatic lobules. It can be noticed that both the values and shapes of the curves in Fig. 6(d) are very similar as those in Fig. 6(c). Firstly, both in forward and backward

Biomedical Optics EXPRESS

measurements the FDH curves of connective tissues are flat and wide, while the FDH curves of hepatic lobules are tall and narrow. The mean values of connective tissues (0.159 in forward and 0.174 in backward) are far larger than those of hepatic lobules (0.043 in forward and 0.055 in backward). Also from Table 1 we can see that the standard deviations of hepatic lobules (0.024 in forward and 0.025 in backward) are smaller than those of connective tissues (0.072 in forward and 0.062 in backward), confirming that the value distribution of retardance for connective tissues is wider than that of hepatic lobule tissues. We also calculated the contrasts of δ parameter, which are 57% and 52% in forward and backward measurements respectively. The very similar retardance value distributions here in backward and forward measurements suggest the similar average optical paths for transmitted and backscattered photons of the 40 μm porcine liver tissue sample. When the thickness of porcine liver tissue sample increases, the average retardance value in backward measurement becomes larger than that in forward measurement [39], indicating longer average optical paths for backscattered photons. However, the contrasts of retardance images are still similar for forward and backward measurements. Moreover, from Table 1 we can observe that the depolarization parameters Δ and $1\text{-}b$, also retardance parameters δ and t_3 have similar contrasts between connective and hepatic lobule tissues. Therefore, the results shown in Fig. 6 and Table 1 quantitatively testify that for the porcine liver sample, the values and distributions of the retardance parameters are very similar in forward and backward measurements. However, for depolarization parameters they have smaller values and larger contrasts in transmission measurements than those in backscattering images.

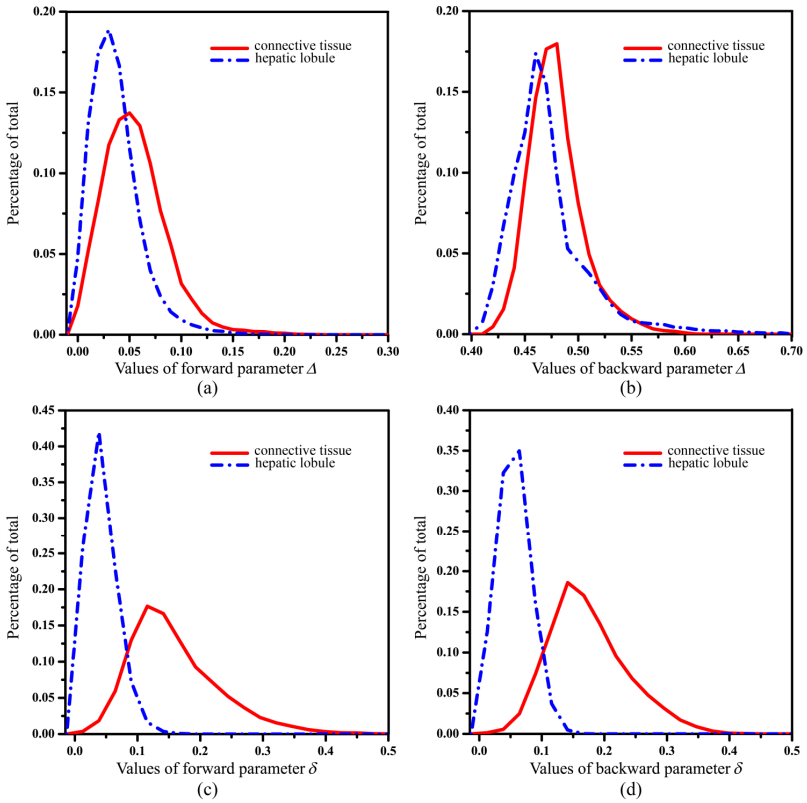

Fig. 6. Frequency distribution histogram of MMPD parameters Δ and δ of porcine liver sample: (a) Δ in forward measurement; (b) Δ in backward measurement; (c) δ in forward measurement; (d) δ in backward measurement. The red solid lines represent connective tissues and blue dotted lines represent hepatic lobules.

Biomedical Optics EXPRESS

Table 1. Mean values and standard deviations of Mueller matrix derived parameters for porcine liver sample

Parameters	*1-b*	*Δ*	t_3	*δ*
Mean values of connective tissues in forward	0.049	0.052	0.148	0.159
Mean values of hepatic lobules in forward	0.038	0.043	0.055	0.043
Mean values of connective tissues in backward	0.422	0.481	0.085	0.174
Mean values of hepatic lobules in backward	0.415	0.467	0.029	0.055
Standard deviation of connective tissues in forward	0.035	0.030	0.062	0.072
Standard deviation of hepatic lobules in forward	0.029	0.024	0.032	0.024
Standard deviation of connective tissues in backward	0.029	0.026	0.031	0.062
Standard deviation of hepatic lobules in backward	0.044	0.038	0.014	0.025

Then, we plot out the FDHs of parameters *Δ* and *δ* for breast carcinoma samples. From the results shown in Fig. 7 and Tab. 2 we can conclude that: (1) Though in backward measurement the values of parameter *Δ* are much larger than in forward measurement, in both forward (Fig. 7(a)) and backward (Fig. 7(b)) measurements, the mean values of parameter *Δ* of fibers (0.0025 in forward and 0.900 in backward) are almost the same as those of non-fibrous tissues (0.0021 in forward and 0.898 in backward), showing no imaging contrast of depolarization between anisotropic and isotropic breast tissues; (2) On the other hand, as Fig. 7(c) and (d) show, there is a similar and prominent imaging contrast of parameter *δ* between fibrous and non-fibrous areas in both forward and backward measurements. The mean values of parameter *δ* in forward measurement are 0.104 for fibers and 0.015 for non-fibrous tissues, while in backward imaging the mean values are 0.340 for fibers and 0.127 for non-fibrous tissues. Moreover, we can see from Table 2 that the standard deviations of the fibrous structures are 0.056 in forward measurement and 0.138 in backward measurement, which are prominently larger than those of the non-fibrous tissues (0.01 in forward and 0.026 in backward measurements). The contrasts of *Δ* and *δ* parameters are 8%, 0.1% and 74%, 46% in forward and backward measurements, respectively. In summary, the results shown in Fig. 7 and Table 2 also indicate that for human breast carcinoma pathological samples, the retardance parameters *δ* and t_3 have similar contrasts between fibrous and non-fibrous areas in both transmission and backscattering imaging. However, due to the limited thickness of tissue samples used for transmission polarimetry, the values of depolarization parameters *Δ* and *1-b* are much smaller compared with backscattering polarimetry. It means the information and indicators useful for diagnosis obtained from transmission Mueller matrix microscope based on retardance of standard pathological tissue slices can also be available for backward *in vivo* polarimetric imaging, including Mueller matrix endoscope.

Biomedical Optics EXPRESS

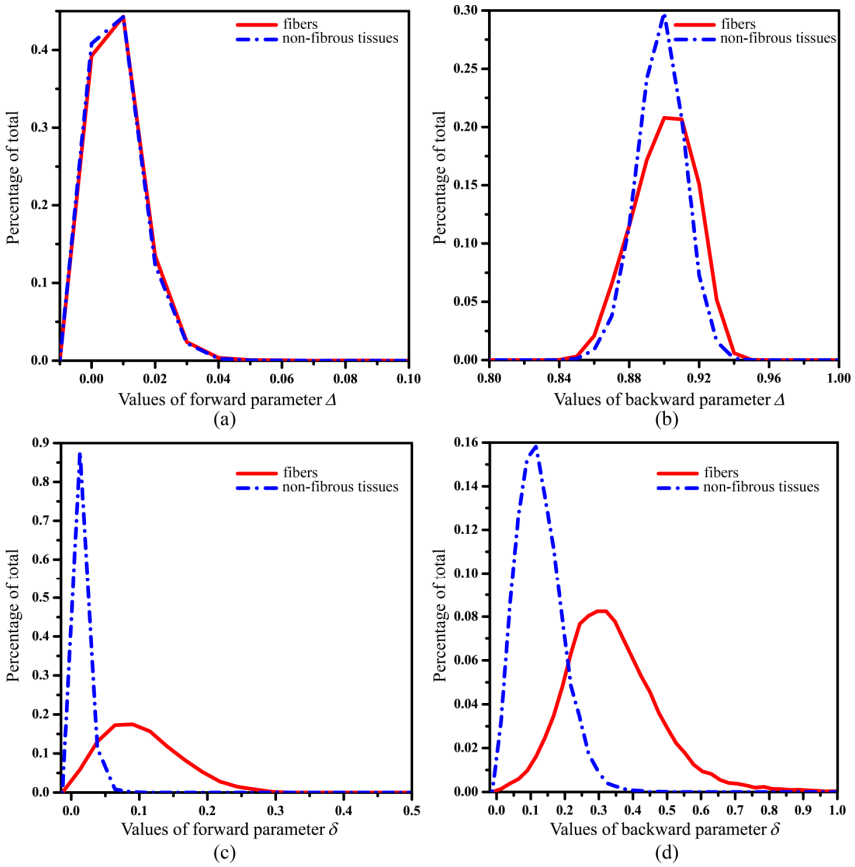

Fig. 7. Frequency distribution histogram (FDH) of MMPD parameters Δ and δ for human breast carcinoma samples. (a) Δ in forward measurement; (b) Δ in backward measurement; (c) δ in forward measurement; (d) δ in backward measurement. The red solid lines represent the fibers and blue dotted lines represent non-fibrous tissues, respectively.

Table 2. Mean values and standard deviations of Mueller matrix derived parameters for human breast carcinoma samples

Parameters	*1-b*	Δ	t_3	δ
Mean values of fibers in forward	0.005	0.0025	0.105	0.104
Mean values of non-fibrous tissues in forward	0.004	0.0021	0.019	0.015
Mean values of fibers in backward	0.869	0.900	0.026	0.340
Mean values of non-fibrous tissues in backward	0.860	0.898	0.012	0.127
Standard deviation of fibers in forward	0.012	0.007	0.056	0.056
Standard deviation of non-fibrous tissues in forward	0.010	0.007	0.012	0.010
Standard deviation of fibers in backward	0.021	0.017	0.012	0.138
Standard deviation of non-fibrous tissues in backward	0.016	0.013	0.007	0.026

3.4 Monte Carlo stimulations

For a better understanding, in this section we carried out MC simulations based on the SBM to compare the Mueller matrix parameters in forward and backward measurements. According to the tissue samples, the parameters used in the MC simulations are set as follows: The values of thickness for the porcine liver sample, human breast carcinoma pathological tissue slice and bulk breast carcinoma tissue are 40 μm, 10 μm and 200 μm. The large spherical scatterers (diameters of 8 μm and scattering coefficient of 150 cm^{-1}) and small spherical scatterers (diameters of 0.5 μm and scattering coefficient of 50 cm^{-1}) mimic the cell nuclei and organelles, respectively [24,48]. The illuminating wavelength is 632 nm. The

Biomedical Optics EXPRESS

refractive indices of the scatterers and interstitial medium are 1.41 and 1.33, respectively. The birefringence values Δn are 0.001 for anisotropic tissue and 0.0001 for isotropic tissue.

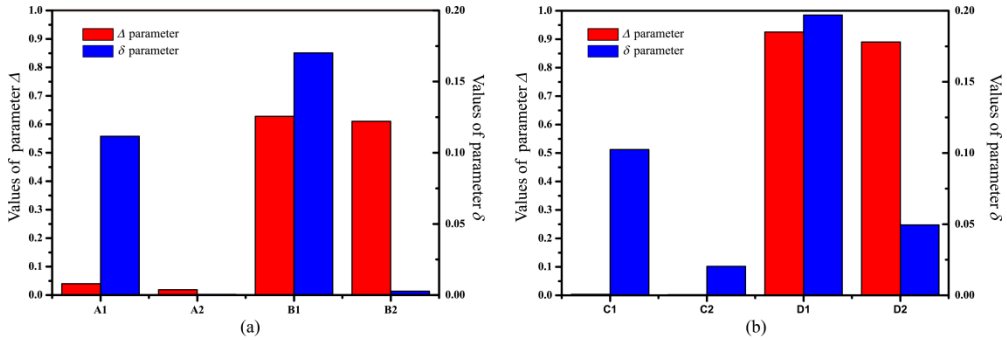

Fig. 8. Monte Carlo simulation results of parameters Δ and δ for: (a) porcine liver tissues and (b) human breast carcinoma tissues. The red and blue columns represent Δ and δ respectively. A1, A2, B1, B2, C1, C2, D1 and D2 represent connective tissue and hepatic lobule in transmission imaging, connective tissue and hepatic lobule in backscattering imaging, fibers and non-fibrous tissues of slices in transmission imaging and fibers and non-fibrous tissues of bulk tissues in backscattering imaging.

Figure 8 provides the MC simulated results of parameters Δ and δ for porcine liver and human breast carcinoma samples in forward and backward measurements. From Fig. 8(a) we can see that the values of depolarization parameter Δ of porcine liver's connective tissue and hepatic lobule are close in both transmission and backscattering simulations. Meanwhile there are significant contrasts of the retardance parameter δ between the connective tissue and hepatic lobules: for both the transmission and backscattered results, the values of anisotropic connective tissues are prominently larger than those of isotropic hepatic lobules. Also as Fig. 8(b) shows, for the breast carcinoma tissues with different thickness both transmission and backscattered results of parameter Δ do not show much difference while parameter δ has significant larger values for fibers. The simulation results are consistent with the experiments above. Here we compared the transmission and backscattering Mueller matrix images of *ex vivo* internal organ tissues. It should be noted that *in vivo* polarimetric biomedical diagnostics often require probing epithelial tissues. Our recent study demonstrated that the structures of epithelial tissues can also be described using the sphere cylinder-birefringence model when analyzing the polarimetric imaging contrasts [36]. It suggested that the Mueller matrix imaging contrasts of epithelial tissues and internal organ tissues are generated from similar structures (e.g. cell nuclei, organelles, fibers). Thus although more studies are still needed, we believe that the conclusion of polarimetric contrasts in transmission and backscattering measurements above still holds for specimens with epithelial tissues.

4. Conclusion

In summary, to compare the imaging contrasts of Mueller matrix polarimetric parameters between transmission and backscattering measurements, in this study we firstly prepared and analyzed porcine liver tissue samples with appropriate thickness to be measured both in forward and backward configurations. Then for a further study on human pathological tissues, we compared the transmission images of thin slices and backscattering images of bulk samples from the same human breast carcinoma tissue specimens. The experiments and corresponding Monte Carlo stimulation results demonstrated that, the backscattering and transmission retardance-related parameters δ and t_3 have very similar contrasts to characterize the anisotropic and isotropic structures of tissues, meaning that the conclusions made from Mueller matrix microscopic imaging based on retardance can also be helpful to guide the *in situ* backscattering Mueller matrix polarimetry diagnosis. However, the values and contrasts of depolarization-related Mueller matrix parameters Δ and *1-b* have some differences between

Biomedical Optics EXPRESS

transmission and backscattering polarimetry. For porcine liver tissues the depolarization parameters may have smaller values and larger contrasts in transmission measurements than those in backscattering images. For pathological samples, due to the limited thickness of tissue slices used for transmission polarimetry, the values of depolarization parameters are much smaller compared with backscattering polarimetry.

Funding

National Key Research and Development Program of China (2016YFF0103000, 2016YFC0208600); the Science and Technology Project of Shenzhen (No. JCYJ20170412170814624); and National Natural Science Foundation of China (NSFC) (No. 61405102, 61527826, 41475125).

Disclosures

The authors declare that there are no conflicts of interest related to this article.